ORIGINAL PAPER

Rate-dependent constitutive modeling of brain tissue

Mohammad Hosseini-Farid[1] · Mohammadreza Ramzanpour[1] · Jayse McLean[1] · Mariusz Ziejewski[1] ·
Ghodrat Karami[1]

Abstract
In this paper, the dynamic behavior of bovine brain tissue, measured from a set of in vitro experiments, is investigated and represented through a nonlinear viscoelastic constitutive model. The brain samples were tested by employing unconfined compression tests at three different deformation rates of 10, 100, and 1000 mm/s. The tissue exhibited a significant rate-dependent behavior with different compression speeds. Based on the parallel rheological framework approach, a nonlinear viscoelastic model that captures the key aspects of the rate dependency in large-strain behavior was introduced. The proposed model was numerically calibrated to the tissue test data from three different deformation rates. The determined material parameters provided an excellent constitutive representation of tissue response in comparison with the test results. The obtained material parameters were employed in finite element simulations of tissue under compression loadings and successfully verified by the experimental results, thus demonstrating the computational compatibility of the proposed material model. The results of this paper provide groundwork in developing a characterization framework for large-strain and rate-dependent behavior of brain tissue at moderate to high strain rates which is of the highest importance in biomechanical analysis of the traumatic brain injury.

Keywords Brain tissue · Constitutive modeling · Strain rate · Parallel rheological framework · Compressibility · Finite element

1 Introduction

Evaluating the mechanical properties of the brain tissue is a fundamental subject in understanding intracranial brain deformation under different loading conditions. It has been shown that severe rotation of the head creates rapid angular acceleration in the brain causing brain deformations and shear strains which may lead to TBI (Holbourn 1943). TBI can also occur from blunt impacts leading to an acute subdural hematoma, diffuse axonal injury (DAI), death, or other serious disability (Faul et al. 2010; O'riordain et al. 2003; Rueda and Gilchrist 2009). To study in vivo intracranial behavior under TBI conditions, FE models have been introduced to predict the brain deformation for different applied loads (Eslaminejad et al. 2018b; Giordano et al. 2014; Goriely et al. 2015b; Hosseini-Farid et al. 2018; Ramazanian

et al. 2018; Ramzanpour et al. 2018; Ratajczak et al. 2019; Raul et al. 2006). In these analyses, while creating a computational model containing detailed anatomical geometries of the human head is necessary, it is also highly important to employ accurate material properties for the intracranial organs. Modeling TBI is dynamic in nature and the brain will experience a variety of loading rates for different scenarios. Thus, for a rate-dependent material such as the brain, it is necessary to select the correct material properties corresponding to a specific simulation rate.

It has been shown that severe brain injury under blunt impact normally occurs when the brain deforms within the strain-rate range of 23–140 s^{-1} (Viano and Lovsund 1999; Zhang et al. 2004). Also, the recent computational studies of various impact and blast scenarios indicated that for mild to severe TBI, the brain undergoes strain rates ranging from 36 to 241 s^{-1} (Farid et al. 2018). It should be noticed that the effective time durations in higher-frequency loads, such as impact-induced and blast-induced TBI, are, respectively, within the order of some and less than one millisecond (Saboori and Walker 2019; Zhang et al. 2004). With such a short

✉ Ghodrat Karami
g.karami@ndsu.edu

1 Department of Mechanical Engineering, North Dakota State University, Fargo, ND 58104, USA

time duration, the rate effect is a key feature in studying the behavior of the brain in TBI-related loading. Substantial studies have focused on characterizing this viscoelastic behavior by using time-dependent stress-strain relations (de Rooij and Kuhl 2016; Hosseini-Farid et al. 2019a; Mendis et al. 1995; Miller 1999). Those studies employed the strain energy functions linearly coupled with time domain to implicitly address the strain-rate effects at large strains (Hosseini-Farid et al. 2019b; Rashid et al. 2012). Although this modeling provides effective constitutive representation for short- and long-term tissue behaviors, calibrating these linear viscoelastic models to test results from various rates is fairly challenging (Farahmand and Ahmadian 2018; Farid et al. 2017). In contrast, limited works in the literature have developed the nonlinear hyper-viscoelastic material models which were phenomenological in nature and have successfully reproduced the rate-dependent tissue responses over complex loading histories (de Rooij and Kuhl 2016). Although the hysteresis and dissipative characteristics were fully addressed by these models, their formulations are not supported in FE packages and are only useful if one is interested in self-developed numerical studies (Haldar and Pal 2018; Prevost et al. 2011).

The aim of this study is to elaborate on some key features of characterizing the brain tissue at high strain rates paving the way for investigating the injury at the central nervous system under dynamical loads. This work is going to be a preliminary step in developing a predictive model for brain tissue over a large variety of strains and strain rates. In the experimental portion of this study, unconfined tests with compression velocities of 10, 100, and 1000 mm/s were carried out on animal brain tissues for strain value of up to 30%. The nonlinear viscoelastic constitutive modeling is described, and the compatibility of the new model for implementation in FE software packages has been examined. This paper establishes an introductory step toward the development of a comprehensive experimental, theoretical, and computational framework to enhance the FE analysis being employed in a variety of biomechanical studies for traumatic brain injury.

2 Materials and methods

2.1 Experiments

Four fresh bovine brains were obtained from the Animal Science Department facilities at North Dakota State University. The animals were 2 years old, and all were healthy. The brains were carefully removed from their heads, immediately kept in phosphate-buffered saline (PBS) solution to prevent dehydration, and transported to the lab cold, but not frozen, to prevent mechanical decay. All tests were conducted within three to eight hours after the slaughtering. First, the samples from the brain were cut from the frontal and parietal lobes of each hemisphere. The procedure followed the experimental protocol by Miller and Chinzei (1997b) instructed to prepare samples for uniaxial unconfined compression tests. The actual measured diameter and height of samples before conducting the experiment were 24.8 ± 0.3 mm and 15.0 ± 0.3 mm (mean $\pm$ SD), respectively. All the extracted brain specimens consisted of a mixture of gray and white matter.

Similar to Rashid et al. (2012), the unconfined compression tests were conducted on the mixed gray and white matter specimens for up to 30% strain of each sample height. Tests were performed at room temperature (~22 °C) using a BOSE 3200 Electroforce machine (BOSE Corporation, Bloomington, MN, USA) designed for testing soft tissue materials. Figure 1 shows the experimental setup of the unconfined compression tests. Before each test, the surfaces of the top and lower platens were thoroughly treated with a surgical lubricant (Surgilube, Fougera Pharmaceuticals Inc.) to establish unconfined compression conditions. This procedure was essential to diminish the frictional effects and to provide a uniform expansion in the radial direction. Samples were then carefully located between the two platens. The outer surface of each brain specimen was carefully humidified with phosphate-buffered saline solution to keep the tissue hydrated, during the entire test procedure. After hydration, the upper platen was cautiously moved downward until it touched the sample. Then, all forces and reference displacement were set to zero. The tests were performed at three different deformation rates of 10 mm/s ($n = 10$ brain samples), 100 mm/s ($n = 8$), and 1000 mm/s ($n = 12$). These compression velocities correspond to approximate nominal strain rates of 0.67, 6.67, and 66.7 s^{-1}. Figure 1 shows the Electroforce machine which was used for the testing. Also, the radial expansion of the cylindrical specimens captured by a high-speed camera (NanoSense MKIII, DantecDynamics) at different instances (Fig. 1) confirmed that the deformation was approximately homogeneous. It proves that employing the surgical lubricant was effective in minimizing the frictional effects between the sample and the platens.

2.2 Constitutive modeling

2.2.1 Preliminaries

The parallel rheological framework allows the introduction of a nonlinear viscoelastic material model consisting of multifold networks connected in parallel (Bergstrom 2015). As shown in Fig. 2, the mechanical response of brain tissue can be decomposed into two parallel networks: hyperelastic equilibrium network (spring), specified as network A, and a rate-dependent viscoelastic behavior (spring–dashpot), defined as network B (Farid 2019).
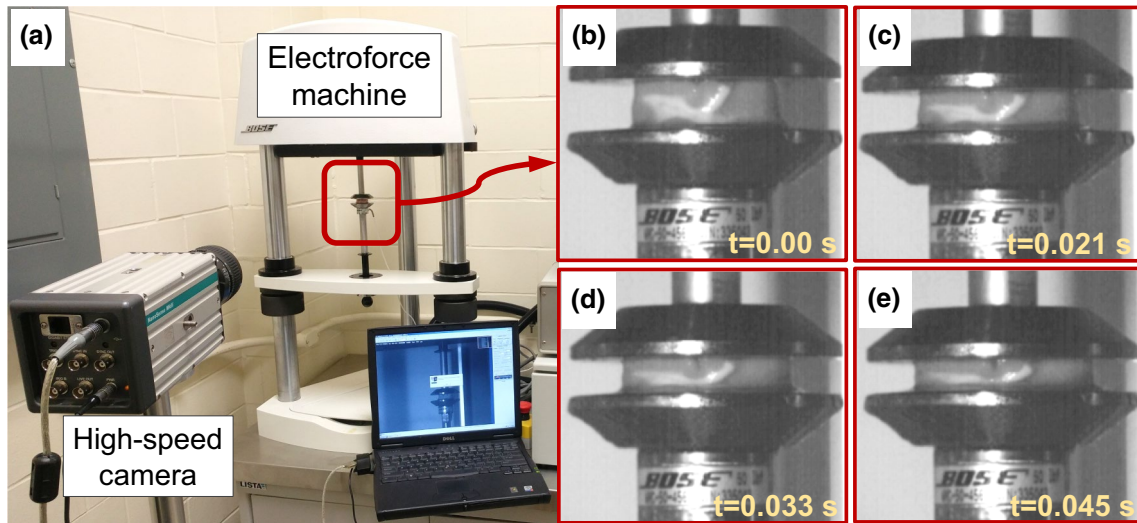
Fig. 1 a Electroforce machine ready for the in vitro unconfined compression test while a high-speed camera records samples deformation, and the deformation steps of brain specimen with speed of 100 mm/s in terms of time at **b** $t=0.00$, **c** $t=0.021$, **d** $t=0.033$, and **e** $t=0.045$ s, corresponding to compressive strain of 0, -0.14, -0.21, and -0.3

Fig. 2 a Schematic representation of the proposed nonlinear viscoelastic model with two parallel networks consisted of an equilibrium network A and a viscoelastic network B, **b** the multiplicative decomposition of the deformation for the rheological components of this model
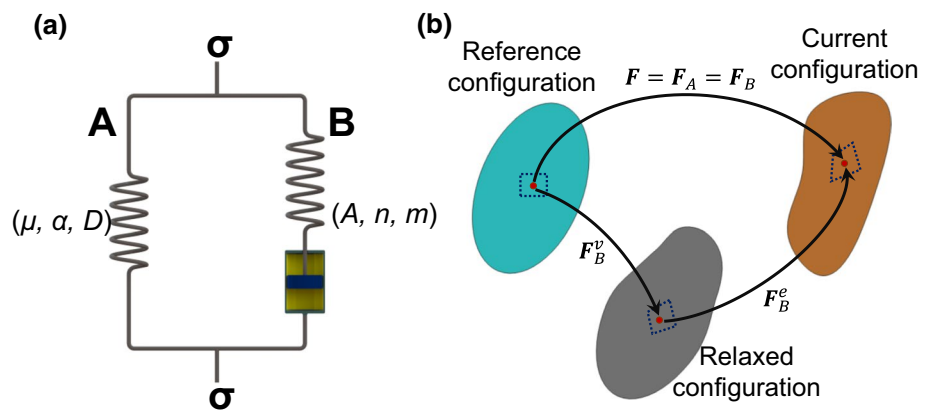
Considering the parallel continuity, for each network the deformation gradient tensor can be considered to be equal:

$$F = F_A = F_B \tag{1}$$

where the deformation gradient F correlates the position of a point at deformed rate-dependent configuration x to its position at undeformed state X as:

$$F = \frac{\partial x}{\partial X} = \nabla \otimes x \tag{2}$$

The deformation gradient tensor introduces the right Cauchy–Green tensor C as $C = F^T \cdot F$. For the kinematic characterization, the deformation gradient (F) and right Cauchy–Green tensor (C) are generally decomposed into volumetric contribution, characterized through the volume change (J) and a deviatoric (isochoric), volume-preserving contribution (Laksari et al. 2012). In this regard, $\bar{F}$ and $\bar{C}$ denote the deviatoric part of deformation and can be written in the form of

$$\bar{F} = J^{\frac{-1}{3}} F, \quad \bar{C} = J^{\frac{-2}{3}} C \tag{3}$$

where J, the Jacobian tensor, represents the change in volume between the deformed and undeformed states, introduced as $J = \det(F) = \lambda^{1-2\nu}$, with λ being the stretch ratio.

2.2.2 Elastic behavior

It is assumed that the equilibrium network response is purely elastic. Any form of strain energy function for expressing the behavior of soft materials can be employed to model the elastic (spring) response in each network. It is assumed that both networks have the same hyperelastic model (Bergstrom 2015;

Goriely et al. 2015a), and the total strain energy, U_T, is obtained from the weighted summation of the energies of two networks

$$U_T = s_1 U\left(C_A^e\right) + s_2 U\left(C_B^e\right) \tag{4}$$

where C_A^e and C_B^e are the elastic right Cauchy–Green tensor in networks A and B. The stiffness ratio of networks, s_i, is a dimensionless material parameter indicating the ratio of shear modulus of networks A and B and must satisfy $s_1 + s_2 = 1$.

The total Cauchy stress response, σ_T, of the system can be derived from the strain energy function as follows:

$$\sigma_T = \sigma_A + \sigma_B = -pI + s_1 \left\{ 2F_A^e \cdot \frac{\partial U\left(C_A^e\right)}{\partial C_A^e} \cdot \left(F_A^e\right)^T \right\} \\ + s_2 \left\{ 2F_B^e \cdot \frac{\partial U\left(C_B^e\right)}{\partial C_B^e} \cdot \left(F_B^e\right)^T \right\} \tag{5}$$

where p is the hydrostatic pressure that is determined by boundary conditions. In this paper, the *Ogden* strain energy function is used to evaluate the elastic response of both networks (Ogden 1972, 1986). The general (compressible) form of the *Ogden* strain energy function is:

$$U_{Ogden} = \sum_{i=1}^{N} \frac{2\mu_i}{\alpha_i^2}\left(\bar{\lambda}_1^{-\alpha_i} + \bar{\lambda}_2^{-\alpha_i} + \bar{\lambda}_3^{-\alpha_i} - 3\right) + \sum_{i=1}^{N} \frac{1}{D_i}(J-1)^{2i} \tag{6}$$

where $\bar{\lambda}_i$ is the deviatoric principal stretch introduced as $\bar{\lambda}_i = J^{-\frac{1}{3}} \lambda_i$, N is the material parameter number, and μ_i, α_i, and D_i are material parameters. The initial shear modulus and bulk modulus for the *Ogden* model are given by $\mu_0 = \sum_{i=1}^{N} \mu_i$ and $K_0 = \frac{2}{D_1}$, respectively. In this study, the compressible form of *Ogden* hyperelastic model is employed to consider the compressibility effect. For this study, the volumetric parameter (D_1) was assessed by using the calculated initial shear modulus, μ_0, and Poisson's ratio, ν, as:

$$D = \frac{2}{K} = \frac{3(1-2\nu)}{\mu_0(1+\nu)} \tag{7}$$

According to Eq. (7), the value for Poisson's ratio (ν) is needed in order to determine the parameter D (Forte et al. 2017; Shojaeiarani et al. 2019). The value of $\nu = 0.49$, reported in substantial number of studies as the Poisson's ratio for the brain tissue (Miller et al. 2000; Tse et al. 2014), was applied to calculate the compressibility parameter of hyperelastic model.

2.2.3 Viscous behavior

The whole viscous behavior is taken into account by network B (Fig. 2a), which is modeled by assuming the multiplicative split of the deformation gradient into both elastic and viscous (inelastic) deformation (Fig. 1):

$$F_B = F_B^e \cdot F_B^v \tag{8}$$

where the viscous part of the deformation, F_B^v, represents the stress-free intermediate configuration of the network B (Quintavalla and Johnson 2004). The elastic component of deformation gradient, F_B^e, is evaluated using its classical form, and F_B^v is calculated via time integration of the rate of creep deformation gradient in the viscoelastic network, $\dot{F}_B^v$. In this regard, the velocity gradient in network B is given by

$$L_B = \dot{F}_B F_B^{-1} \tag{9}$$

It is similarly decomposed into the elastic and inelastic components given as:

$$L_B = \left[\frac{d}{dt}\left(F_B^e \cdot F_B^v\right)\right]\left(F_B^e \cdot F_B^v\right)^{-1} \\ = \left[\dot{F}_B^e \cdot F_B^v + F_B^e \cdot \dot{F}_B^v\right]\left(F_B^v\right)^{-1}\left(F_B^e\right)^{-1} \tag{10}$$

which can be written as

$$L_B = \dot{F}_B^e\left(F_B^e\right)^{-1} + F_B^e \cdot \dot{F}_B^v\left(F_B^v\right)^{-1}\left(F_B^e\right)^{-1} \tag{11}$$

and with respect to Eq. (9), Eq. (11) will be written in the form of

$$L_B = L_B^e + F_B^e \cdot L_B^v \cdot \left(F_B^e\right)^{-1} = L_B^e + \tilde{L}_B^v \tag{12}$$

where

$$L_B^v = D_B^v + W_B^v \quad \text{and} \quad \tilde{L}_B^v = \tilde{D}_B^v + \tilde{W}_B^v \tag{13}$$

It is assumed that the system possesses an unchanged rotation in the intermediate relaxed configuration regarding to the stress-free state (reference configuration) (Boyce et al. 1989); therefore, the viscous spin tensor becomes zero, $\tilde{W}_B^v = 0$. Thus, the viscous rate of deformation in network B is constitutively represented by the symmetric part of the velocity gradient as $\tilde{L}_B^v = \tilde{D}_B^v$. To describe the viscoelastic constitutive response of deformation gradient, the evolution of the creep part is considered ($\tilde{D}_B^v \equiv D^{cr}$) (Hurtado et al. 2013). Hence, through the multiplicative split of the deformation gradient for isotropic materials suggested by (Lee 1969) the rate form of creep deformation gradient is rewritten as (Dafalias 1986):

$$\dot{F}_B^v = \left(F_B^e\right)^{-1} \cdot D^{cr} \cdot F_B^e \cdot F_B^v \tag{14}$$

where D^{cr} is expressed based on creep potential, $G^{cr} = G^{cr}(\sigma)$, and proportionality factor, $\dot{\lambda}$, and the flow rule is given as:

$$D^{cr} = \dot{\lambda} \frac{\partial G^{cr}(\sigma)}{\partial \sigma} \tag{15}$$

In this model, we assume the creep potential is characterized by $\bar{q}$, the equivalent deviatoric Cauchy stress, as $G^{cr} = \bar{q}$, and also the proportionality factor is defined

as $\dot{\lambda} = \dot{\bar{\varepsilon}}^{cr}$, where $\dot{\bar{\varepsilon}}^{cr}$ is the equivalent creep strain rate. Therefore, the flow rule will be given by

$$\boldsymbol{D}^{cr} = \frac{3}{2\bar{q}} \dot{\bar{\varepsilon}}^{cr} \overline{\boldsymbol{\sigma}} \quad \text{or} \quad \boldsymbol{D}^{cr} = \frac{3}{2\tilde{q}} \dot{\bar{\varepsilon}}^{cr} \overline{\boldsymbol{\tau}} \tag{16}$$

where $\bar{\boldsymbol{\sigma}}$ is the deviatoric Cauchy stress, $\boldsymbol{\tau} = J\boldsymbol{\sigma}$ is the Kirchhoff stress, $\bar{\boldsymbol{\tau}}$ is the deviatoric Kirchhoff stress, and $\tilde{q} = J\bar{q}$. The expression of equivalent creep strain rate, $\dot{\bar{\varepsilon}}^{cr}$, can be provided by models such as power law (Jaishankar and McKinley 2013), power-law strain hardening (Dalrymple et al. 2015; Ghoreishy and Sourki 2018), hyperbolic sine law (Hurtado et al. 2013), or either from Bergstrom–Boyce (Bergström and Boyce 2001). In this paper, $\dot{\bar{\varepsilon}}^{cr}$ is defined based on power-law strain-hardening model in the form of

$$\dot{\bar{\varepsilon}}^{cr} = (A\tilde{q}^{\boldsymbol{n}}[(m+1)\bar{\varepsilon}^{cr}]^m)^{\frac{1}{m+1}} \tag{17}$$

where $\bar{\varepsilon}^{cr}$ is the equivalent creep strain and A, m, and n are the material parameters.

2.3 Parameter identification

All experimental data from three different loading rates of unconfined compression tests for bovine brain tissue were simultaneously used for calibrating the material parameters. The nonlinear least-squares algorithm *lsqnonlin* in MATLAB was employed to identify the constitutive constants of the proposed material model. To achieve a physically meaningful amount for material constants, the shear modulus, μ_1, and A were constrained to have an only positive value. Also, Eq. (7) with the value of $\nu = 0.49$ stands as the constraints for determining the volumetric parameter, D_1. At each iteration, this parameter was first calculated from the estimated shear modulus based on Eq. (7) and then employed into the optimization process. The objective function (χ^2) which represents the sum of the square of the difference between experimental and numerically calculated stresses is defined as follows:

$$\chi^2 = \sum_{k=1}^{3} \sum_{i=1}^{N} \left(\sigma_i^{\text{Exp}} - \sigma_i^{\text{Num}} \right)^2 \tag{18}$$

where σ_i^{Num} and σ_i^{Exp} are the numerically predicted and experimentally measured true (Cauchy) stresses, respectively, for three loading rates ($k = 1$–3) and N is the number of data points. To accelerate the parameter identification process, it is essential to assign a restricted range for each parameter value. Therefore, in this regard the parameters m and n were set to be calculated from the range of [0.5, 10] and [−1,0], respectively. Eventually, one set of material parameters that provided the best fit to the test results of the brain at three measured rates were obtained.

3 Results

3.1 Mechanical response of brain tissue

Based on force and displacement signals obtained directly from the testing machine, the force histories versus the compressive strains were determined and are presented in Fig. 3. To attain the stress-strain behavior of the bovine brain shown in Fig. 3d, the Lagrangian stresses were calculated by dividing the force over the initial cross-sectional area of the sample measured at its reference configuration. The averaged nominal stress-strain curves were determined by up to 30% of compressive strain, showing an inherent nonlinear mechanical behavior of tissue at each deformation rate. The brain tissue showed a stiffer response when the compression rate increased (Fig. 3d), indicating that the stress not only is a function of strain value but also depends on the loading rate.
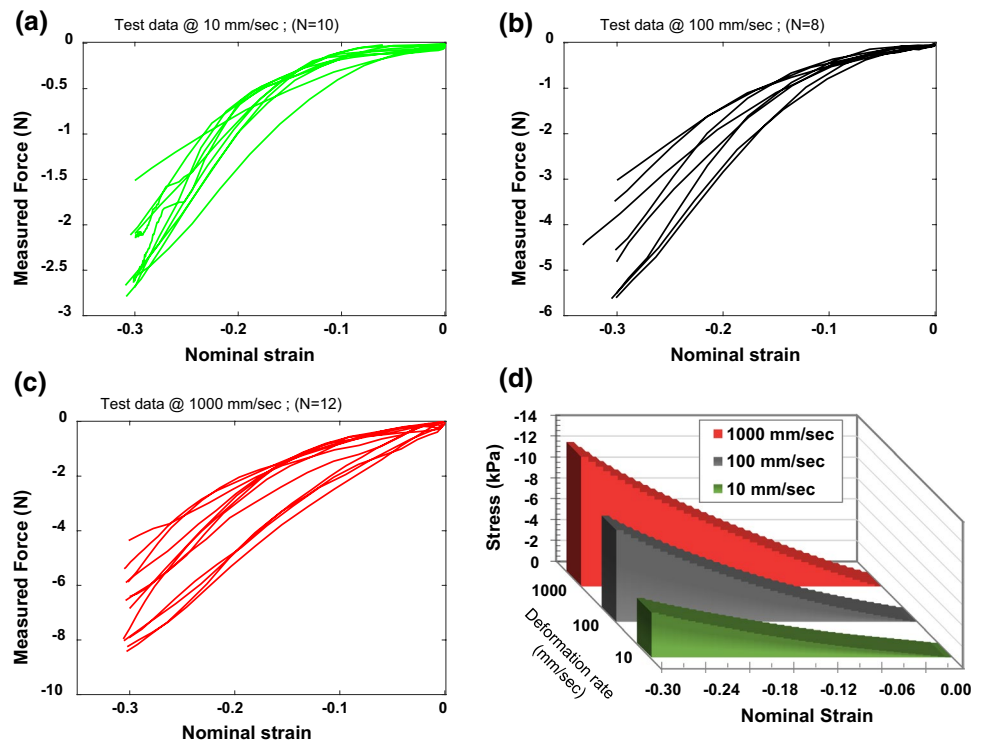
The maximum nominal stresses at 30% compressive strain with the deformation rates of 10, 100, and 1000 mm/s are -4.26 ± 1.26 kPa, -8.62 ± 2.58 kPa, and $-12.74.0 \pm 3.97$ kPa (mean $\pm$ SD), respectively. According to one-way ANOVA (SPSS Statistics, version 24.0, IBM Corp., Armonk, NY) (Eslaminejad et al. 2018a; Jahani et al. 2018), the values of nominal stress at 30% strain showed significant statistically different ($p < 0.01$) over various deformation rates (Fig. 4). The apparent elastic modulus (slope of stress-strain curve) at 5%, 10%, 15%, and 20% strains for different compression velocities was determined and is compared in Fig. 4. A consistent rise in the elastic modulus was observed with increasing the strain levels and strain rates. As shown in Fig. 4, this measure of mechanical stiffness demonstrated a statistical difference and significant rate-dependent behavior for brain tissue.

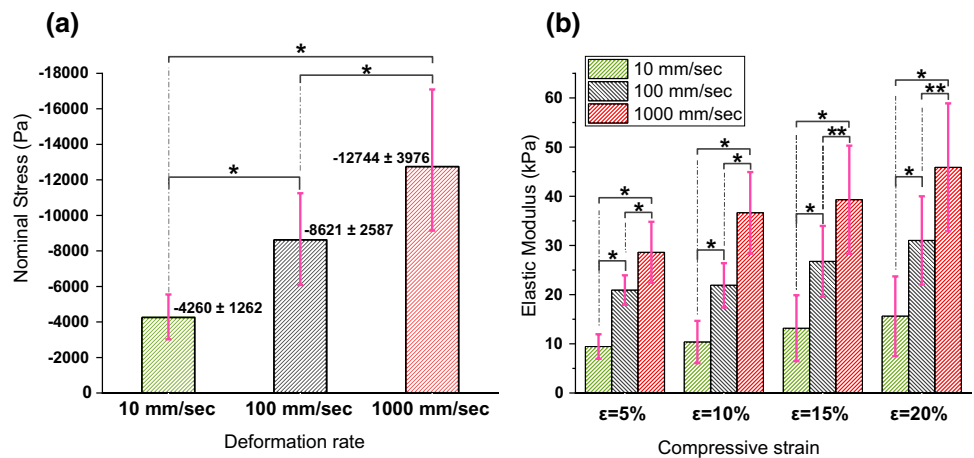### 3.2 Determined rate-dependent material parameters

Table 1 presents the summary of determined material constants of the proposed model for bovine brain tissue at three different rates. The calculated weighted factors (s_i) of hyperelastic stress in the first and second networks were found to be 0.273 and 0.727, respectively. Both deviatoric (μ) and volumetric (D) constitutive parameters of the *Ogden* hyperelastic model were evaluated. This nonlinear viscoelastic model provided excellent constitutive representation in comparison with the test data for brain tissue ($R^2 = 0.999$). Figure 5 demonstrates the prediction of the proposed model for the mechanical response of brain tissue at three deformation rates of 10, 100, and 1000 mm/s.

Fig. 3 The experimentally recorded history of forces vs. nominal compressive strain for bovine brain specimens at different compression velocities of **a** 10 mm/s, **b** 100 mm/s, and **c** 1000 mm/s, and **d** the comparison between mean nominal stresses measured at three different compression velocities

Fig. 4 a The maximum nominal stress (mean $\pm$ SD) determined at 30% compressive strain exhibits significant difference ($p < 0.01$) at various deformation rates. **b** Also, the estimated elastic moduli as a measure of apparent stiffness increased by the rise in the strain level and the strain rate. * and ** represent statistical difference using ANOVA, with the significance level set at $p < 0.01$ and $p < 0.05$, respectively

Table 1 Material parameters for the nonlinear viscoelastic model, calibrated for brain tissue at different deformation rates of 10, 100, and 1000 mm/s

Matter	Material parameters							R^2_{Tot}
	Hyperelastic parameters			Rate-dependent parameters				
	μ_1 (Pa)	α_1	D_1 (Pa^{-1})	s	A (Pa^{-n}s^{-m-1})	n	m	
Brain	2941	1.58	1.37e−5	0.727	0.02429	0.5875	−0.1828	0.999

3.3 Model verification in finite element analysis

In order to check the validity of the introduced model and the obtained material parameters for use in FE analysis, an inverse simulation of test procedure was carried out. Using

ABAQUS/Standard 2016 code (ABAQUS Inc., Providence, RI), the same unconfined compression experiment was modeled by the FE technique for a brain specimen. As shown in Fig. 6a, an axisymmetric geometry with a radius of 12.5 mm and a height of 15 mm was generated resembling the brain

Fig. 5 The comparison between experimental data and the determined mechanical response by nonlinear viscoelastic model for brain tissue at three different rates of: **a** 10 mm/s, **b** 100 mm/s, and **c** 1000 mm/s
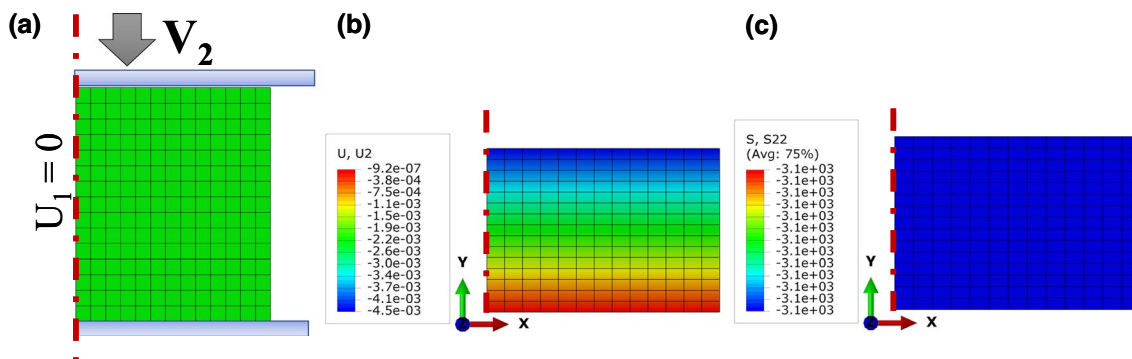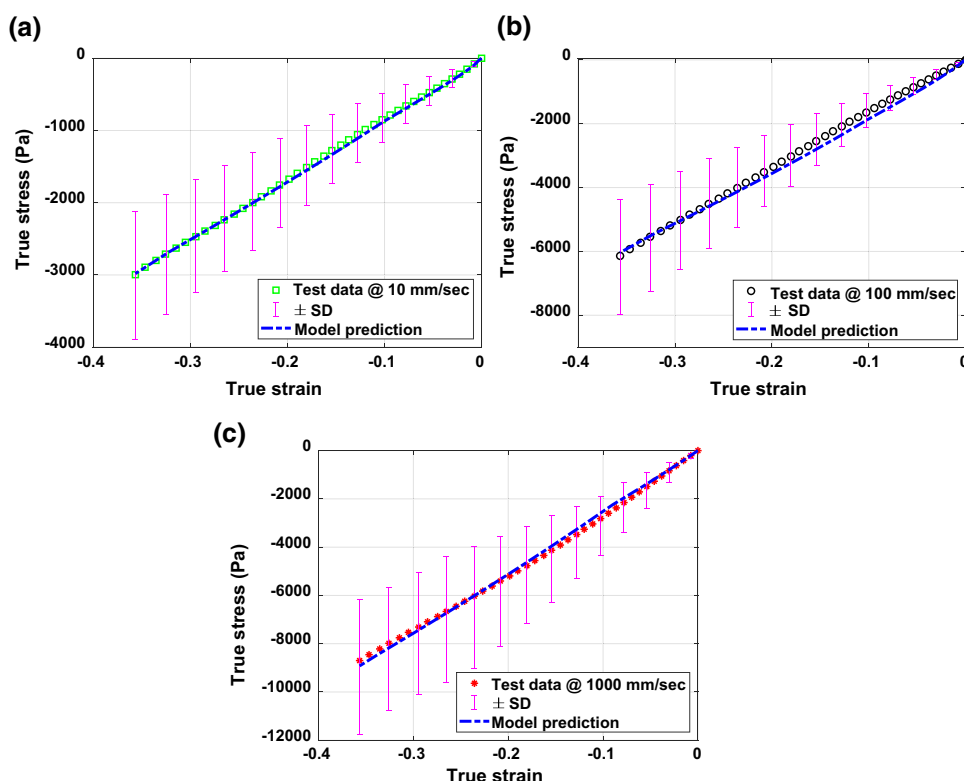

Fig. 6 **a** The developed FE model for unconfined compression test procedure of the brain specimen, **b** the homogeneous deformation configuration of tissue at 30% of compressive strain, and **c)** the con-tour of Cauchy stress in "Y–Y" (vertical) direction for the sample compressed up to $\varepsilon = -0.3$ strain with velocity of 10 mm/s

specimen. A four-node, axisymmetric quadrilateral, reduced integration, hybrid element, which includes hourglass control, was employed. On the left rotational axis, an axisymmetric boundary condition ($U_1 = 0$) was applied. A frictionless interaction was applied between platens and the top and bottom surfaces of the brain sample. The constitutive constants presented in Table 1 were implemented as the material properties of tissue in the FE model (see "Appendix"). The upper platen was moved in the vertical direction, compressing the specimen to 30% of its engineering strain with three deformation rates used in the experiments (i.e., 10, 100, 1000 mm/s). A uniform uniaxial deformation along with

homogenous radial expansion was observed for the brain sample as depicted in Fig. 6b. That leads to fully uniaxial compression stress in vertical ("Y–Y") direction with insignificant transverse stress in the radial direction (Fig. 6c).

As depicted in Fig. 7, very good agreements between experimentally measured stress-strain and FE computed results were achieved for brain sample at three different tested speeds. In order to obtain the nominal stresses in the FE analysis shown in Fig. 7, the calculated reaction force for the upper platen was divided by the initial top area of the brain sample. Also, additional simulations with velocities in the range of calibrated rates (10 ~ 1000 mm/s)
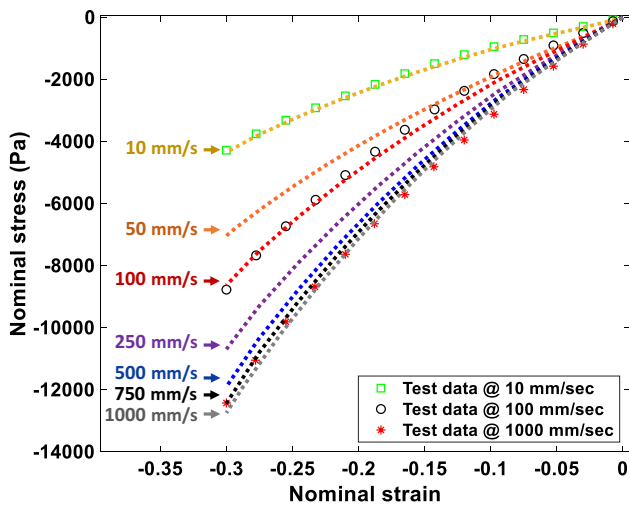
Fig. 7 The predicted nominal stress by FE analysis of brain sample (dotted lines) with different deformation rates using the material constants presented in Table 1

were chosen to further examine the validity of the model and determined material parameters. In this regard, the FE simulations were performed for the compressive speeds of 50, 250, 500, and 750 mm/s, and the computed tissue response for each rate is presented in Fig. 7. This rate-dependent model gives proper predictions of the tissue response for other intermediate rates. The calculated mechanical responses in Fig. 7 and the predicted deformed configuration in Fig. 6 were in full agreement with experimental results, verifying the validity of the proposed material model to reproduce the tissue viscoelastic behavior.

Similar to other engineering parameters, the developed strain rates in the brain specimens can be calculated by FE analysis. The results of the FE simulation show the brain has a uniform distribution of strain rates. As demonstrated in Fig. 8, at the strain value of 30% and for the compression velocity of 10, 100, and 1000 mm/s, the vertical strain rates (ER22) were found to be, respectively, -0.94, -9.4, and $-94\ s^{-1}$. These values were negative since they are related to compressive deformations and strains. The transversal strain-rate components in "X–X" and "Z–Z" directions (ER11 and ER33) were identical and with a value of $46\ s^{-1}$ at the speed of 1000 mm/s. It can be seen that the estimated strain rate associated with the highest compression velocity of this study is consistent with those reported ranges of rates at TBI (Viano and Lovsund 1999; Zhang et al. 2004). Although for constant velocity, it was expected to obtain the constant strain rate, the calculated strain rate showed some variations at different strains. These variations for both lateral and vertical strain rates (ER11 and ER22) versus the compressive strains are demonstrated and depicted in Fig. 8c, d.

4 Discussion

The main objective of this study was to verify and calibrate the rate-dependent model on the animal brain, and further pave the path for determining the most accurate material properties of human brain. In this regard, the rate-dependent mechanical behavior of bovine brain tissue has been investigated under unconfined compression test at intermediate to high rates. Figure 4 reveals how the peak stress and the

Fig. 8 The demonstration of determined strain rate: **a** the strain-rate contour in the direction of "Y–Y" plotted for 30% of strain, **b** symbol plot of strain-rate components at three directions plotted for 30% of strain, **c** the variation of strain rate in transversal direction versus strain, **d** the variation of strain rate in vertical direction versus strain

apparent elastic modulus of the bovine brain vary as the rate changes. Based on the parallel rheological framework approach, a single-phase nonlinear viscoelastic model was developed and calibrated with the experimental result. The averaged experimental results at three different rates were employed to determine one set of material parameters. The excellent agreement between the numerically calculated and experimentally measured stresses (Fig. 5a–c) confirmed that the proposed constitutive model is fully capable of characterizing the rate-dependent behavior of brain tissue under compression deformation.

The researchers of the study presented here could not find any studies with perfectly similar deformation rates of the bovine brain tissue to compare their results with. However, good agreement was found between the results of the current study and the results provided by Laksari et al. (Laksari et al. 2012). In that study, engineering stress of 10.3 kPa (at $\varepsilon = -0.3$) was reported for bovine brain samples under unconfined compression test at the nominal strain rate of 10 s^{-1}. Pervin and Chen (2009) were able to examine the mechanical responses of the bovine brain at high rates using a modified split Hopkinson pressure bar. They obtained insignificant anisotropy behavior for white matter and showed the compressive stress at 30% strain with a nominal strain rate of 1000/s was 60 and 75 kPa for gray and white matter, respectively. Although Rashid et al. (2012) have examined porcine brain tissue, they determined the compressive stresses as 8.8, 12.8, and 16 kPa (at $\varepsilon = -0.3$) corresponding to compression velocities of 150, 300, and 450 mm/s. These varying ranges were typical in the results of experimental studies. These are likely due to the fact that the samples were obtained from different animal species and ages, and prepared in different shapes and dimensions, and tested with different protocols (e.g., lubrication, preloading, etc.) (Anderson 2018; Elkin et al. 2010).

In the literature of biomechanics of the brain, some studies have been devoted to characterizing the rate-dependent mechanical properties of this tissue. Pamidi and Advani (1978) derived a nonlinear constitutive relation based on power energy function. They calibrated their model using the reported in vitro test results of Galford and McElhaney (1970) and obtained a good numerical prediction of human brain tissue under compression. Mendis et al. (1995) have developed a large-strain linear viscoelastic model to be used in finite element modeling of brain tissue. They incorporated the Prony series into the Mooney–Rivlin strain energy function and determined the time-dependent form of the hyperelastic coefficient. Miller and Chinzei (1997b) implemented a similar hyper-viscoelastic model to characterize the viscoelastic behavior of porcine brain tissue. They introduced a unique procedure to calculate the material constants over three different low to medium rates. Hrapko et al. (2006) captured the nonlinear mechanical response of brain under

the shear response of tissue, using a new differential viscoelastic model that was developed based on Mooney–Rivlin viscoelastic network and included 16 material parameters. In order to capture the rate-dependent behavior at finite viscosity and deviatoric and volumetric plasticity of the brain tissue, El Sayed et al. (2008b) developed a nonlinear elastic–viscoplastic material model and verified their model with tissue response under uniaxial compression and tension test up to 50% nominal strain. Also, Prevost et al. (2011) have investigated the dynamic behavior of porcine brain tissue at nominal strain rates of 0.01, 0.1, and 1 s^{-1}. They developed a rheology-based constitutive model to capture the effects of compressibility, hysteresis conditioning, the rate dependency, and short- and long-term viscoelastic behaviors of the tissue. Although their comprehensive model with eight parameters was proven to predict the behavior of tissue at tension, and relaxation modes as well, it has a limited ability for being used in FE software packages. Recently, Haldar and Pal (2018) developed a rate-dependent anisotropic constitutive relation and numerically modeled the brain tissue under large deformation. They have shown that their rigorous phenomenological model was able to account for the rate dependency, nonlinear viscoelasticity, anisotropy, and tension-compression asymmetry behavior of the tissue.

Although the model proposed in this study accounts for the compressibility effect of tissue deformation, it has fewer material constants to be determined in contrast to existing constitutive models which lead to a relatively faster model calibration process and less computational cost. Also, it was shown that the developed nonlinear viscoelastic model can be directly implemented in commercial FE code to perform the FE simulations with no need for writing a material subroutine. In this regard, the main features of this model in comparison with the most common viscoelastic models used to characterize the rate-dependent behavior for brain tissue are presented in Table 2.

The present study is an essential step toward the development of a constitutive model able to predict the tissue behavior during large deformation at arbitrary loading velocities. As the limitations of the current study, it should be noted that the tissue was characterized for only uniaxial deformation (unconfined compression) over a range of intermediate to high rates. If the material parameters are determined for one particular deformation mode such as compression, it may not exhibit adequate behavior for other deformation modes such as tension, shear, or other loading combinations. One other limitation of this study is the estimation of the material parameters from a mixed white and gray matter of the brain tissue. The results, therefore, are only valid for such a composite and can be useful in approximate modeling of the brain (Miller and Chinzei 1997a; Rashid et al. 2012). Also, we have assumed an isotropic structure and employed the average mechanical properties of the tissue

Table 2 A summary of most well-known rate-dependent constitutive models have been introduced to characterize the brain viscoelastic behavior in comparison with the model proposed in this study

Reference study/model	Key feature	No. of material constants	Compressibility	FE availability
Pamidi and Advani (1978)/power energy function	Rate dependent	3	N.A.	N.A.
Mendis et al. (1995) and Miller and Chinzei (1997b)/linear hyper-viscoelastic	Time dependent	8	N.A.	Yes
Bergström and Boyce (2001)/nonlinear hyper-viscoelastic	Rate dependent	8	Yes	Yes
Hrapko et al. (2006)/nonlinear viscoelastic	Rate dependent	16	N.A.	Yes*
El Sayed et al. (2008b)/nonlinear elastic–viscoplastic	Rate dependent	13	Yes	Yes**
Prevost et al. (Prevost et al. 2011)/nonlinear hyper-viscoelastic	Rate dependent	8	Yes	N.A.
Haldar and Pal (2018)/nonlinear hyper-viscoelastic	Rate dependent	8	N.A.	N.A.
This study/nonlinear hyper-viscoelastic	Rate dependent	7	Yes	Yes

*This model is available in the explicit finite element code MADYMO (Hrapko et al. 2009)

**It seems the model has not becoming available in commercial FE packages, yet (El Sayed et al. 2008a)

in the determination of material parameters; however, this procedure is accepted in obtaining such parameters that are useful in evaluating an approximate behavior of the tissue. Moreover, in some studies, it was postulated that the anatomical location (Donnelly and Medige 1997; Tamura et al. 2007) and the direction (Budday et al. 2017; Pervin and Chen 2009) of extracted brain samples had an insignificant effect on the tissue response. For instance, Tamura et al. (2007) have performed several unconfined compression tests and have shown that neither the orientations nor anatomical location of the specimen do not affect the macro-mechanical behavior of porcine brain tissue.

As a suggestion for future work, further model refinement is required to address the time-dependent viscoelastic behavior associated with the biphasic inherent of brain tissue at intermediate to high deformation rate regime. This single-phase viscoelastic model provided here was a first step toward achieving this goal, and it is needed to introduce a viscoelastic biphasic constitutive model to demystify more phenomenological behavior of brain tissue. It is suggested in the next step that brain tissue is treated as a porous medium, composed of a solid matrix with interstitial fluid, and the significant role of fluid diffusion in the brain tissue is taken into account. On this subject, the future biphasic constitutive model should be able to capture the tissue rate-dependent behavior resulting from the coupled dynamical interactions between the mechanical response of the solid phase and fluid flow.

5 Conclusions

This study demonstrates the in vitro results for bovine brain tissue in unconfined compression experiments up to 30% nominal strain over three orders of deformation rate magnitudes (10–1000 mm/s). The significant effects for rate dependency of this soft biological tissue were observed. It was shown that with an increase in deformation rate, the mechanical features, i.e., the nominal stress and apparent elastic moduli, were also increased. A rate-dependent constitutive relation was introduced and simultaneously calibrated with the measured data from three various rates of deformation. The excellent correlations between the experimental, theoretical, and computational results have indicated that the proposed model is fully able to characterize brain tissue behavior and be employed in FE simulations. The outcome of this study is a promising constitutive model and a successful technique to capture the rate-dependent material properties, a complex inherent characteristic of the brain at intermediate to high strain rates.

Appendix

Modeling parallel rheological framework in ABAQUS

Parallel rheological framework (PRF) is a finite-strain constitutive approach, which is referred to model nonlinear viscoelasticity, Mullins effect, and permanent set in polymers and elastomeric materials. The framework is made from the superposition of elastic or elastoplastic networks in parallel with one or multiple finite-strain viscoelastic network, N (Fig. 9). This material model has been available in ABAQUS 6.13 and later versions (ABAQUS/Standard User's Manual, version 6.13; Providence, RI). This framework can be consisted of arbitrary number of viscoelastic networks and is able to (1) use a hyperelastic
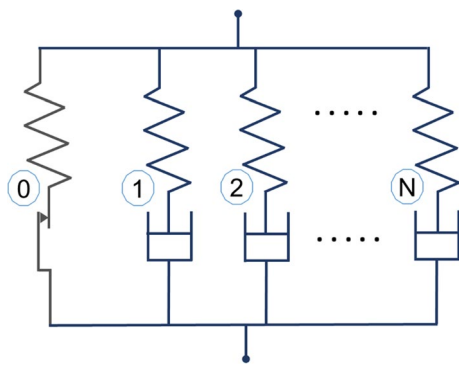
Fig. 9 Schematic representation of the parallel rheological framework with *N* viscoelastic networks in parallel with an elastoplastic network

material model to specify the elastic response; (2) be combined with Mullins effect to predict material softening; (3) incorporate nonlinear kinematic hardening with multiple back stresses in the elastoplastic response; and (4) employ multiplicative split of the deformation gradient and a flow rule derived from a creep potential to specify the viscous behavior.

A variety of hyperelastic models (e.g., Mooney–Rivlin, neo-Hookean, Ogden, polynomial, Yeoh, etc.) in combination with various common creep laws (i.e., power law, strain-hardening power law, hyperbolic sine, Bergstrom–Boyce) or even with a user-defined creep model led to introduce a diverse material models for representing the complex viscoelastic behavior for materials.

Assign strain-hardening power-law model in ABAQUS

ABAQUS command *Viscoelastic*, *Nonlinear*, *LAW = STRAIN* was used to define the nonlinear viscoelastic model based on the strain-hardening power-law formulation. The strain-hardening power law is defined by specifying three material parameters: *A*, *n*, and *m*. To obtain physically reasonable behavior, *A* and *n* must be positive and $-1 < m \leq 0$. In this study, the calibrated material model is implemented as the form of the ABAQUS inp-file format that is shown in the following:

```
**MATERIALS
**
*Material, name=Ogden-Strain-Law
*Hyperelastic, Ogden
2941., 1.58, 1.37 e−5
**
*Viscoelastic, Nonlinear, NetworkId=1, SRatio=0.727, Law=strain
0.02429, 0.5875, −0.1828
```

References

Anderson PS (2018) Making a point: shared mechanics underlying the diversity of biological puncture. J Exp Biol 221:jeb187294

Bergstrom JS (2015) Mechanics of solid polymers: theory and computational modeling. William Andrew, Norwich

Bergström J, Boyce M (2001) Constitutive modeling of the time-dependent and cyclic loading of elastomers and application to soft biological tissues Mechanics of materials 33:523–530

Boyce MC, Weber G, Parks DM (1989) On the kinematics of finite strain plasticity. J Mech Phys Solids 37:647–665

Budday S et al (2017) Mechanical characterization of human brain tissue. Acta Biomater 48:319–340

Dafalias Y (1986) Erratum:"The Plastic Spin" (Journal of Applied Mechanics, 1985, 52, pp. 865–871). J Appl Mech 53:290

Dalrymple T, Hurtado J, Lapczyk I, Ahmadi H (2015) Parallel rheological framework to model the amplitude dependence of the dynamic stiffness in carbon-black filled rubber. Const Models Rubber IX:189

de Rooij R, Kuhl E (2016) Constitutive modeling of brain tissue: current perspectives. Appl Mech Rev 68:010801

Donnelly B, Medige J (1997) Shear properties of human brain tissue. J Biomech Eng 119:423–432

El Sayed T, Mota A, Fraternali F, Ortiz M (2008a) Biomechanics of traumatic brain injury. Comput Methods Appl Mech Eng 197:4692–4701

El Sayed T, Mota A, Fraternali F, Ortiz M (2008b) A variational constitutive model for soft biological tissues. J Biomech 41:1458–1466

Elkin BS, Ilankovan A, Morrison B (2010) Age-dependent regional mechanical properties of the rat hippocampus and cortex. J Biomech Eng 132:011010

Eslaminejad A, Hosseini-Farid M, Ramzanpour M, Ziejewski M, Karami G (2018a) Determination of mechanical properties of human skull with modal analysis. In: ASME 2018 international mechanical engineering congress and exposition. American Society of Mechanical Engineers, pp V003T004A097–V003T004A097

Eslaminejad A, Hosseini Farid M, Ziejewski M, Karami G (2018b) Brain tissue constitutive material models and the finite element analysis of blast-induced traumatic brain injury. Sci Iran 25:3141–3150

Farahmand F, Ahmadian M (2018) A novel procedure for micromechanical characterization of white matter constituents at various strain rates. Sci Iran. https://doi.org/10.24200/sci.2018.50940.1928

Farid MH (2019) Mechanical characterization and constitutive modeling of rate-dependent viscoelastic brain tissue under high rate loadings. North Dakota State University

Farid MH, Eslaminejad A, Ziejewski M, Karami G (2017) A study on the effects of strain rates on characteristics of brain tissue. In: ASME 2017 international mechanical engineering congress and exposition, 2017. American Society of Mechanical Engineers, pp V003T004A003–V003T004A003

Farid MH, Eslaminejad A, Ramzanpour M, Ziejewski M, Karami G (2018) The strain rates of the brain and skull under dynamic Loading. In: ASME 2018 international mechanical engineering congress and exposition, 2018. American Society of Mechanical Engineers, pp V003T004A067–V003T004A067

Faul M, Xu L, Wald MM, Coronado VG (2010) Traumatic brain injury in the United States, Centers for Disease Control and Prevention, National Center for Injury Prevention and Control, Atlanta, GA

Forte AE, Gentleman SM, Dini D (2017) On the characterization of the heterogeneous mechanical response of human brain tissue. Biomech Model Mechanobiol 16:907–920

Galford JE, McElhaney JH (1970) A viscoelastic study of scalp, brain, and dura. J Biomech 3:211–221

Ghoreishy MHR, Sourki FA (2018) Development of a new combined numerical/experimental approach for the modeling of the non-linear hyper-viscoelastic behavior of highly carbon black filled rubber compound. Polym Test 70:135–143

Giordano C, Cloots R, Van Dommelen J, Kleiven S (2014) The influence of anisotropy on brain injury prediction. J Biomech 47:1052–1059

Goriely A, Budday S, Kuhl E (2015a) Chapter two-neuromechanics: from neurons to brain. Adv Appl Mech 48:79–139

Goriely A et al (2015b) Mechanics of the brain: perspectives, challenges, and opportunities. Biomech Model Mechanobiol 14:931–965

Haldar K, Pal C (2018) Rate dependent anisotropic constitutive modeling of brain tissue undergoing large deformation. J Mech Behav Biomed Mater 81:178–194

Holbourn A (1943) Mechanics of head injuries. The Lancet 242:438–441

Hosseini-Farid M, Ramzanpour M, Eslaminejad A, Ziejewski M, Karami G (2018) Computational simulation of brain injury by golf ball impacts in adult and children. Biomed Sci Instrum 54:369–376

Hosseini-Farid M, Ramzanpour M, Ziejewski M, Karami G (2019a) A compressible hyper-viscoelastic material constitutive model for human brain tissue and the identification of its parameters. Int J Non-Linear Mech 116:147–154

Hosseini-Farid M, Rezaei A, Eslaminejad A, Ramzanpour M, Ziejewski M, Karami G (2019b) Instantaneous and equilibrium responses of the brain tissue by stress relaxation and quasi-linear viscoelasticity theory. Sci Iran 26:2047–2056

Hrapko M, van Dommelen JAW, Peters GWM, Wismans JSHM (2006) The mechanical behaviour of brain tissue: large strain response and constitutive modeling. Biorheology 43:623–636

Hrapko M, Van Dommelen J, Peters G, Wismans J (2009) On the consequences of non linear constitutive modelling of brain tissue for injury prediction with numerical head models. Int J Crashworthiness 14:245–257

Hurtado J, Lapczyk I, Govindarajan S (2013) Parallel rheological framework to model non-linear viscoelasticity, permanent set, and Mullins effect in elastomers. Const Models Rubber VIII95:95–100

Jahani B, Salimi Jazi M, Azarmi F, Croll A (2018) Effect of volume fraction of reinforcement phase on mechanical behavior of ultra-high-temperature composite consisting of iron matrix and TiB2 particulates. J Compos Mater 52:609–620

Jaishankar A, McKinley GH (2013) Power-law rheology in the bulk and at the interface: quasi-properties and fractional constitutive equations. Proc R Soc A Math Phys Eng Sci 469:20120284

Laksari K, Shafieian M, Darvish K (2012) Constitutive model for brain tissue under finite compression. J Biomech 45:642–646

Lee EH (1969) Elastic-plastic deformation at finite strains. J Appl Mech 36:1–6

Mendis KK, Stalnaker RK, Advani SH (1995) A constitutive relationship for large deformation finite element modeling of brain tissue. J Biomech Eng 117:279–285

Miller K (1999) Constitutive model of brain tissue suitable for finite element analysis of surgical procedures. J Biomech 32:531–537

Miller K, Chinzei K (1997a) Constitutive modeling of brain tissue: experiment and theory. J Biomech 30:1115–1121

Miller K, Chinzei K (1997b) Constitutive modelling of brain tissue: experiment and theory. J Biomech 30:1115–1121

Miller K, Chinzei K, Orssengo G, Bednarz P (2000) Mechanical properties of brain tissue in vivo: experiment and computer simulation. J Biomech 33:1369–1376

O'riordain K, Thomas P, Phillips J, Gilchrist M (2003) Reconstruction of real world head injury accidents resulting from falls using multibody dynamics. Clin Biomech 18:590–600

Ogden RW (1972) Large deformation isotropic elasticity–on the correlation of theory and experiment for incompressible rubberlike solids. Proc R Soc Lond A 326(1567):565–584

Ogden R (1986) Recent advances in the phenomenological theory of rubber elasticity. Rubber Chem Technol 59:361–383

Pamidi M, Advani S (1978) Nonlinear constitutive relations for human brain tissue. J Biomech Eng 100:44–48

Pervin F, Chen WW (2009) Dynamic mechanical response of bovine gray matter and white matter brain tissues under compression. J Biomech 42:731–735

Prevost TP, Balakrishnan A, Suresh S, Socrate S (2011) Biomechanics of brain tissue. Acta Biomaterialia 7:83–95

Quintavalla S, Johnson S (2004) Extension of the Bergstrom–Boyce model to high strain rates. Rubber Chem Technol 77:972–981

Ramazanian T, Müller-Lebschi JA, Chuang MY, Vaichinger AM, Fitzsimmons JS, O'Driscoll SW (2018) Effect of radiocapitellar Achilles disc arthroplasty on coronoid and capitellar contact pressures after radial head excision. J Shoulder Elbow Surg 27:1785–1791

Ramzanpour M, Eslaminejad A, Hosseini-Farid M, Ziejewski M, Karami G (2018) Comparative study of coup and contrecoup brain injury in impact induced TBI. Biomed Sci Instrum 54:76–82

Rashid B, Destrade M, Gilchrist MD (2012) Mechanical characterization of brain tissue in compression at dynamic strain rates. J Mech Behav Biomed Mater 10:23–38

Ratajczak M, Ptak M, Chybowski L, Gawdzińska K, Będziński R (2019) Material and structural modeling aspects of brain tissue deformation under dynamic loads. Materials 12:271

Raul J-S, Baumgartner D, Willinger R, Ludes B (2006) Finite element modelling of human head injuries caused by a fall. Int J Legal Med 120:212–218

Rueda MF, Gilchrist MD (2009) Comparative multibody dynamics analysis of falls from playground climbing frames. Forensic Sci Int 191:52–57

Saboori P, Walker G (2019) Brain injury and impact characteristics. Ann Biomed Eng 47(9):1982–1992

Shojaeiarani J, Hosseini-Farid M, Bajwa D (2019) Modeling and experimental verification of nonlinear behavior of cellulose nanocrystals reinforced poly (Lactic Acid) composites. Mech Mater 135:77–87

Tamura A, Hayashi S, Watanabe I, Nagayama K, Matsumoto T (2007) Mechanical characterization of brain tissue in high-rate compression. J Biomech Sci Eng 2:115–126

Tse KM, Lim SP, Tan VBC, Lee HP (2014) A review of head injury and finite element head models. Am J Eng Technol Soc 1:28–52

Viano DC, Lovsund P (1999) Biomechanics of brain and spinal-cord injury: analysis of neuropathologic and neurophysiology experiments. Traffic Inj Prev 1:35–43

Zhang L, Yang KH, King AI (2004) A proposed injury threshold for mild traumatic brain injury Transactions-American Society of Mechanical Engineers. J Biomech Eng 126:226–236